An image-based approach for structure investigation and 3D numerical modelling of polymeric foams

Stefano Tagliabue[1]*, Luca Andena[1,2], Michele Nacucchi[3], Fabio De Pascalis[3]

[1] Politecnico di Milano, Dipartimento di Chimica, Materiali e Ingegneria Chimica "Giulio Natta", Piazza L. Da Vinci, 32, Milano (Italy)

[2] Politecnico di Milano, Engineering, Exercise, Environment, Equipment for Sport (E4Sport) Lab, Piazza L. Da Vinci, 32, Milano (Italy)

[3] ENEA, Division for Sustainable Materials, Research Centre of Brindisi, S.S. 7 Appia – km 706, 72100 Brindisi, Italy

* Corresponding author:
Stefano Tagliabue
Politecnico di Milano, Dipartimento di Chimica, Materiali e Ingegneria Chimica "Giulio Natta"
Piazza Leonardo da Vinci 32, 21033, Milano, Italy
e-mail address: stefano.tagliabue@polimi.it
ORCID: 0000-0003-2044-2618

Abstract

Polymeric expanded materials are of great importance in many engineering applications. Despite this, as of today the development of models able to describe the mechanical behaviour of these material as a function of their microstructure is still an open challenge. In this study an image-based approach is proposed for both microstructure characterisation and 3D numerical mechanical simulations. Microstructure is investigated through different algorithms, such as Mean Intercept Length and Autocorrelation function, to determine synthetic parameters able to describe the internal structure. A novel algorithm has been developed to convert the images obtained from computed tomography into a finite element mesh with an optimized number of elements: this method preserves the original structure and can also be used to generate other fictitious structures that can be analysed. The investigation led to the identification of general relationships between foam microstructure and relevant macroscopic physical and mechanical properties. These relationships can serve as a tool to optimize foam morphology or product final properties for several different engineering applications.

Keywords

Polymeric foam; Microstructure; X-Ray Computed micro-Tomography (μ-CT); Mean Intercept Length (MIL); Autocorrelation Function (ACF); Finite Element Modelling (FEM);

1. Introduction

In the last decades polymeric foams found successful employment in many fields of engineering applications, ranging from acoustic and thermal insulation to shock absorption (packaging and sport equipment) and structural applications (core in sandwich panels). Thermoplastic polymers are commonly used to produce foams thanks to their permeability to expanding gases (e.g. CO_2) in the molten state [26]. Despite the large use of thermoplastics in the last years many other polymeric systems (e.g. rigid crosslinked, elastomers) are used in foams production, with varying production techniques (e.g. gas foaming, extrusion, pressure release) available for the different categories [19, 27, 32, 46].

From a mechanical point of view the compressive behaviour of these materials is commonly divided in three successive stages: in the first one, at low strain levels, they exhibit a linear or quasi-linear response up to a stress value for which the internal structure begins to collapse; the stress then levels off with subsequent strain increase. In this so-called plateau region, foams display their maximum energy absorption capabilities. A third stage, commonly called densification, begins once the internal structures is almost totally collapsed and cell walls come in contact with each other; the behaviour of the foamed materials eventually approaches that of their constituent bulk polymer [13-14]. The evolution of this peculiar mechanical behaviour is strongly related to the characteristics of the internal structure of the foamed polymer: solid fraction, spatial distribution and orientation, cell morphology (open vs. closed) and many other geometrical aspects, but also obviously the intrinsic mechanical properties of the constituent polymer, which are in turn affected by the specific foaming process used [15]. By optimizing the aforementioned characteristics, the resulting structure can be tailored to specific applications (e.g. maximizing absorbed energy makes the foams suitable for sports

equipment or packaging). Many authors in the past years performed an extensive experimental characterization of the compressive mechanical behaviour of different foamed polymers and its dependence on different variables (e.g. [3-4, 40-43]) such as their constituent polymers, applied strain rate and temperature, solid volume fraction and many other aspects.

This wide range of applications prompted many authors, during the past years, to develop models able to describe and predict foams' mechanical behaviour. These models can be divided, based on their approach to the problem, in three main groups:

- *Analytical approach*: with this approach the internal structure of the foam is represented by a regular repetitive unit cell of well-defined geometry and a closed solution can be found under simple loading conditions [13].
- *Voronoi approach*: a series of different random structures are generated, and the mechanical behaviour is analysed with the support of finite element models [11, 25].
- *Image-based approach*: in this case the real geometry of the foams is considered [8, 9], thanks to the most recently available imaging techniques (e.g. X-ray computed tomography (CT) [29], solid state nuclear magnetic resonance) and the acquired set of images serves as a basis to recreate the geometry within a finite element code [12, 31, 35].

Despite the large number of available models and approaches, many critical issues, shared between the different categories, still need to be addressed. The analytical approach suffers from an oversimplification of the structure: the assumption of a regular unit cell is too far from the reality of many polymeric foams. The most commonly used cells are the hexahedron [13], the tetrakaidekahedron [37] and the Kelvin one [16]. The analytical solution for the resulting structure, represented as a set of beams, hinges and proper boundary conditions, usually overestimates the effective mechanical properties of a real foam. The Voronoi approach allows the generation of random structures which do not suffer from oversimplification but display a behaviour that is not necessarily close to the real one [11]. The image-based approach in turn considers the actual structure of the foam under investigation, however at the price of a very high computational cost. Many approximations are often required to strike a reasonable compromise between the need of having a representative volume with a suitable structure description and an affordable global computational cost. These compromises usually lead to simulations of very small volumes of interest, which fail to represent the foam structure at a scale large enough to allow practical applications of the models [12].

The aim of the present work is to develop an efficient image-based approach able to adequately describe the internal structure of polymeric foams inspected with high-resolution CT and convert the imaged structure into a finite element mesh to perform finite element analyses, through suitable algorithms. Since the foam structure is one of the main factors that influences its macroscopic mechanical properties the present investigation focusses on the relevant effects of parameters such as the solid fraction, mean structure thickness and pore size distribution. The spatial distribution of these parameters is investigated using two different tensorial approaches based on the now classic Mean Intercept Length (MIL) and Autocorrelation Function (ACF). The acquired set of images also works as a starting point for finite element mesh reconstruction and subsequent mechanical finite element analysis. Through the development of a custom algorithm a relatively large volume, in the order of a hundred mm^3, can be easily reconstructed and mechanical simulations thus be performed with a

reasonable computational effort. Basic relationships between structure parameters and mechanical properties can then be derived.

The paper is organized as follows: in section 2 (*Theoretical background*) a formal analytical description of both tensorial approaches employed to investigate structure anisotropy is presented. In section 3 (*Experimental methods*) the materials and the experimental techniques used are described while section 4 (*Numerical methods*) deals with the employed numerical methods and algorithms. In section 5 (*Results*) experimental and numerical results are both presented; in this section the influence of the structure on the mechanical response of the foams under investigation is revealed. In section 6 (*Discussion*) a brief discussion on the obtained results is provided and in section 7 (*Conclusions*) the main outcomes of the present work are presented.

2. Theoretical background

2.1 Mean Intercept Length (MIL)

Evaluation of the mean intercept length (MIL) is probably the most common technique to compute fabric tensors related to spongy materials like cancellous bones or polymeric foams [17, 34]. To do so, the method relies on the identification of the phase interfaces and is classified accordingly as boundary-based method [22].

To describe anisotropy using the classical MIL approach, a set of parallel lines along a large number of different directions (ω) in 3D is superimposed on the volume V(x,y,z) (x:0-L,y:0-M,z:0-N) containing the binarized object. The number of intersections with phase interfaces, I(ω), along any one of these lines is then evaluated. MIL as a function of ω can finally be computed as:

$$MIL(\omega) = \frac{h}{I(\omega)} \tag{1}$$

where *h* is the summation of the length of all traced lines. The MIL for the different directions can be plotted in a rose diagram and this 3D diagram can be fitted with an ellipsoid whose parameters define a second rank tensor [17]. This tensor is symmetric, and its eigenvalues and eigenvectors decomposition provide insights about the predominant object orientations. Figure 1 shows an example of the global result obtainable with the calculation of the MIL, represented as a cloud of points in the space.

Cowin [6, 7, 24] defined a MIL fabric tensor as the inverse square root of the MIL tensor of Harrigan and Mann. The advantage of this modification is that the tensor eigenvalues are the values of the mean intercept length measured along the main directions, whereas in the former representation of Harrigan and Mann this relation is essentially the reciprocal one. Again, an ellipsoid can be fitted to the data in three dimensions and its axes can be determined. The data can be also processed using a covariance calculation to define an orientation matrix from which a fabric tensor is derived. The latter method does not assume *a priori* that the data spatial distribution is ellipsoidal [20]. On the other hand, if this distribution can be reasonably fitted with an ellipsoid then there is strict correspondence between the lengths of its axes and the eigenvalues of the covariance matrix, used to determine

ellipsoid orientation [30]. With this approach, the degree of anisotropy (DA) can be computed as the ratio of the maximum to the minimum eigenvalues (λ_{max} and λ_{min}):

$$DA = \frac{\lambda_{max}}{\lambda_{min}} \qquad (2)$$
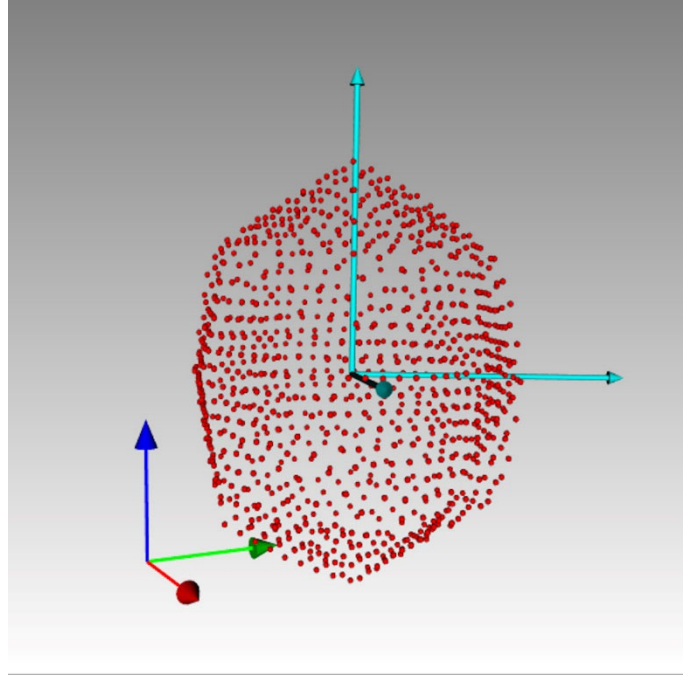
Fig. 1 Example of a cloud of MIL points related to one of the analysed foams (PET 130). The three eigenvectors of the tensor are also drawn in light blue colour with their length proportional to the corresponding eigenvalues.

2.2 Autocorrelation Function (ACF)

The second method to characterize foam morphology is based on the study of the spatial autocorrelation function (ACF) of the CT-tomogram. The ACF method is texture-based: it assumes that the sample possesses a quasi-regular structure that can be described through a suitable fabric tensor [22]. Its validity is still debated in the literature. Wald [33] proposed ACF as a valid alternative to the MIL, finding a fair agreement between the two methods. On the contrary, Tabor [30] found that MIL and ACF approaches are not in general related.

The spatial autocorrelation function related to the 3D binarized volume V(x,y,z) can be expressed as:

$$ACF(x, y, z) = \frac{1}{LMN} \sum_{l=0}^{L} \sum_{m=0}^{M} \sum_{n=0}^{N} V^*(l, m, n) V(x + l, y + m, z + n) \qquad (3)$$

Where V^* denotes the complex conjugate of V but, being V real, the two coincide.

The implementation of the ACF with the integration formula of equation (3) over the entire volume is computationally very expensive; therefore, the autocorrelation was performed exploiting the convolution theorem and applying a Fast Fourier Transform:

$$ACF = IFFT\big(S(f)\big) \qquad (4)$$

where IFFT represents the inverse of the Fast Fourier transform, and S(f) the power spectrum in the frequency domain that can be computed as the product between the Fourier transform of V and its conjugate [9]:

$$S(f) = FFT(V)FFT^*(V) \tag{5}$$

The FFT imposed the conversion of the dataset from 8bit to 32 bit-float [45]. As a consequence, this solution, while faster, is also more demanding in terms of memory space.

Following the method proposed by Wald [33], once the three-dimensional ACF was computed, the full width at half maximum (FWHM) of the autocorrelation function was measured along a series of lines starting from the ACF maximum, always present in its centre, and having directions ω. The directions were established by uniformly sampling the unit sphere. Then, as explained above, a rose diagram was plotted, and a second rank tensor was computed. The diagonalization of the tensor returns its three principal components (eigenvectors) and their related eigenvalues, while the degree of anisotropy is again obtained from equation (2).

3. Experimental methods

3.1 Materials

The material used in the present work is a closed-cell polyethylene terephthalate (PET) foam commonly employed as a core in composite sandwiches for structural applications. Four different nominal densities were considered, and the materials were provided in the form of sheets, foamed by extrusion, of nominal dimensions 150x100x10 mm. Table 1 summarizes the relevant information about the four foams.

<p align="center">Table 1 PET foam nominal densities</p>

Code	Nominal apparent density [kg/m^3]
PET 80	80
PET 100	100
PET 130	130
PET 320	320

3.2 Gas Pycnometry

Foams' apparent density was measured according to ASTM standards [1] with a gas pycnometer *Pycnomatic ATC Thermo Scientific*. Three cubic specimens of 10 mm side length for each foam were prepared; the same sample geometry was also employed for the uniaxial mechanical compression tests. The measurement was performed under pure helium atmosphere (Helium 5.0) at 23°C and at an equilibrium pressure of 2 kPa. The extra-small configuration of the instrument's chamber volume (4 cm^3) was selected. Three consecutive measurements on each specimen were performed to measure the effective volume at the equilibrium. The samples used for this analysis were the same ones employed for X-ray computed tomography.

3.3 Differential Scanning Calorimetry

Differential scanning calorimetry (DSC) was performed to quantify the crystallinity degree of the foams' constituent material according to ISO standards [2] with a *Mettler Toledo - DSC 30*. For each foam two specimens weighting between 5 and 10 mg were heated under a pure nitrogen atmosphere from 30°C to 300°C with a constant heating rate of 10 °C/min. The normalized reference value adopted for 100% PET crystallinity was 140 J/g [36].

3.3 X-ray Computed Tomography

All the tomographic acquisitions were performed by a *GE Phoenix Nanotom CT system* equipped with a 180 kV/15 W nano focus X-ray tube and a 12-bit 2300 x 2300 pixel Hamamatsu flat panel detector. A molybdenum target, suitable for weak absorbing specimens, was used for all the analyses. The accelerating voltage and the beam current of the X-ray tube were 50 kV and 180 μA respectively. The number of projections was 2400. The voxel size was set to 3 μm for each sample (geometric magnification of about 17 times). The exposure time for each projection and the total scan time were 1 sec and four and a half hours, respectively. The volume reconstruction was carried out with the proprietary reconstruction application software *Phoenix datos|x 2*. This software enables to transform the series of acquired X-rays projections, as the sample revolves 360°, in a resulting stack of slices representing the actual digital volumetric reconstruction, via the filtered backprojection algorithm. The size of the datasets was 1300x1300x1300 voxels, corresponding to an investigated volume of 3.9^3 mm^3. The 3D visualization and analysis software *Avizo 8 Fire Edition* by *Visualization Sciences Group* was used for the image processing of the datasets. In order to characterize the cell foam features, the following, typical, processing steps were performed: denoising of grey-scale images by median filter, segmentation by interactive thresholding, pore separation and labelling by watershed algorithm, removal of all the pores touching the borders of the image and, finally, calculation of cell features [8]. Two cubic samples for each nominal density were analysed to assess the representativeness of the investigated volumes and the reproducibility of the adopted analysis techniques.

3.4 Compression Tests

Uniaxial compression tests were performed on cubic specimens with 10 mm side length. The specimens were cut with a band saw (*Proxxon 24260*) and the outer surfaces were sanded to increase surface planarity. Five specimens for each foam were tested with an electromechanical dynamometer *Instron 1185R5800* equipped with a 10 kN load cell, under crosshead displacement control configuration. All the tests were run at 23°C and 50% relative humidity. Preliminary tests were conducted up to a nominal strain of 50% to explore the overall foam mechanical behaviour and identify the range of linear elastic response. After these preliminary tests three specimens per density were compressed along three orthogonal directions up to 2% strain. Displacement data were corrected according to machine compliance, independently measured with ad hoc tests performed using the same setup. All the specimens were tested at a quasi-static strain rate equal to 0.005 s^{-1}, corresponding to a crosshead speed of 3 mm/min.

4. Numerical methods

Images sets acquired with the X-ray computed tomography were used as the basis for structure analysis, performed in terms of solid volume fraction, structure thickness, pores characteristic dimensions and volume anisotropy, and the subsequent finite element mesh reconstruction. Each image represents a slice, i.e. a virtual section, of the acquired CT volume.

4.1 Structure analysis

Starting from the binarized sets of images the solid volume fraction Φ, strictly related to the macro porosity, was easily computed as follows:

$$\Phi = \frac{\# \, Voxel_{full}}{\# \, Voxel_{Tot}} \tag{6}$$

where $\# \, Voxel_{Tot}$ is the total number of voxels within the analysed volume and $\# \, Voxel_{full}$ is the total number of voxels associated with the presence of material in the binarized image after the segmentation stage (Boolean value equal to 1).

Mean structure thickness and pores size were evaluated with the aim to find the foams internal cells characteristic dimensions, as reported by many authors in literature [13]. The average structure thickness was calculated using the algorithm proposed by Hildebrand and Ruesgsegger [18] and implemented in *ImageJ*, while the labelling analysis tool of *Avizo* was used for all cell measurements, including the pore size.

The analysis of anisotropy was accomplished through a custom-made software developed using the *VTK library* [28]. In the implementation used in the current work for both used methods (ACF and MIL), the number of sampled directions was obtained by following the procedure first proposed by Ketcham and Ryan [20]: a sphere is divided into triangular facets that are defined by recursively subdividing the faces of an octahedron and then projecting them outward to the sphere surface. This yields a sample of oriented directions and allows to draw the rose diagrams shown in the results section. In all these figures, the three orthogonal axes x, y, and z are represented with the red, green and blue colours, respectively. The number of orientations chosen for the analysis was 2049.

4.2 Finite element mesh reconstruction

Binarized image sets were also employed for the finite element mesh reconstruction, to numerically reproduce the real geometry of the inspected samples. The well-known marching cube algorithm was implemented in a custom code developed with *Matlab R2019b* [21]. Each binarized pixel, with a Boolean value equal to 1 (representing a solid material region) was converted into a voxel type cubic finite element. The algorithm also kept track of the nodal coordinates (x, y, z) of each finite element, the relative spatial association of the nodes and of the finite elements to which they belong to, and the relative spatial positions of each element with respect to its neighbours. With this information the incidence and coordinates matrixes could be built to import the reconstructed geometry, as a finite element mesh, into a commercial finite element code. In this work *ABAQUS 2018* was used and the reconstructed geometry was thereby imported as an orphan mesh, made up of cubic linear finite elements (C3D8). The characteristic dimension of each element matched exactly the resolution employed during the x-ray computed tomography analysis of the samples (3 μm).

4.2.1 Mesh Optimization

Straightforward application of the marching cube algorithm would result in a huge finite element mesh with hundreds of millions of elements, with an unaffordable computational cost. A new algorithm was developed and implemented in the custom Matlab code to reduce this cost, while preserving the morpho-structural characteristics of the imaged specimens in the whole reconstructed volume. This two-parameters algorithm is freely inspired to the Peano's theory of n-order tensors reduction and is very efficient from a computational point of view.

The two employed parameters are:

- **P** represents the cubic sub-domain side-length in which the 3D tensor, representing the set of binarized images, is subdivided. This is called Peano's number and it assumes positive integer values major or equal to 1. Obviously for P = 1 the image set remains exactly the same. All the defined sub-regions will collapse in a new single voxel with a length size equal to the old resolution (3 μm, in this work) multiplied by P. This product gives the characteristic length scale of the representative volume element of the homogenized medium used to compute the elastic properties.
- **Th** is a threshold. The collapsed region will result in a new voxel representing solid material (Boolean value equal to 1) or its absence (Boolean value equal to 0) according to this parameter. If the ratio of "solid" ones to the total number of voxels within a given sub-region is greater than **Th** the new voxel will be solid (Boolean equal to 1); otherwise its Boolean value will be set to 0.

Starting from high-resolution CT data, and by properly tuning the above described parameters the same CT inspected volume was converted into a finite element mesh with a manageable size.

4.3 Finite Element Model (constitutive law, boundary conditions, output evaluations)

The combination of Peano's and marching cubes algorithms allowed the generation of 20 different finite element meshes of equivalent total volume, subsequently imported in the commercial code *ABAQUS 2018* to perform mechanical finite element simulations. 8 structures represent the real foam samples inspected with the CT and then compressed; the other 12 represent fictitious structures generated with Peano's algorithm by altering the solid fraction, mean structure thickness and degree anisotropy of the real ones. The meshes are made up of a number of cubic linear elements (C3D8) varying from 150000 to 820000. The adopted material constitutive law was linear elastic, with ~~the~~ relevant parameters reported in Table 2.

Table 2 Linear elastic parameters

Parameter	Value
Young's modulus (E)	2900 MPa
Poisson's ratio (v)	0.4

The value of Young's modulus was chosen considering reference data [44] for the constituent material in accordance with the degree of crystallinity measured by differential scanning calorimetry.

Displacement boundary conditions were applied to simulate a uniaxial compression test, up to a nominal strain value of 2% (as in the experiments). Zero displacement was enforced on one face along the compression direction while on the opposite face a total displacement, corresponding to the final aforementioned strain level, was applied.

For all the reconstructed geometries three simulations reproducing experimental compression tests along the three main orthogonal directions were conducted and the relevant apparent moduli were computed. The simulations were run on a Linux machine with 24 cores and 49 GB RAM; the average CPU time needed for a single simulation varied between 2 and 6 hours, depending on the total number of finite elements in the mesh.
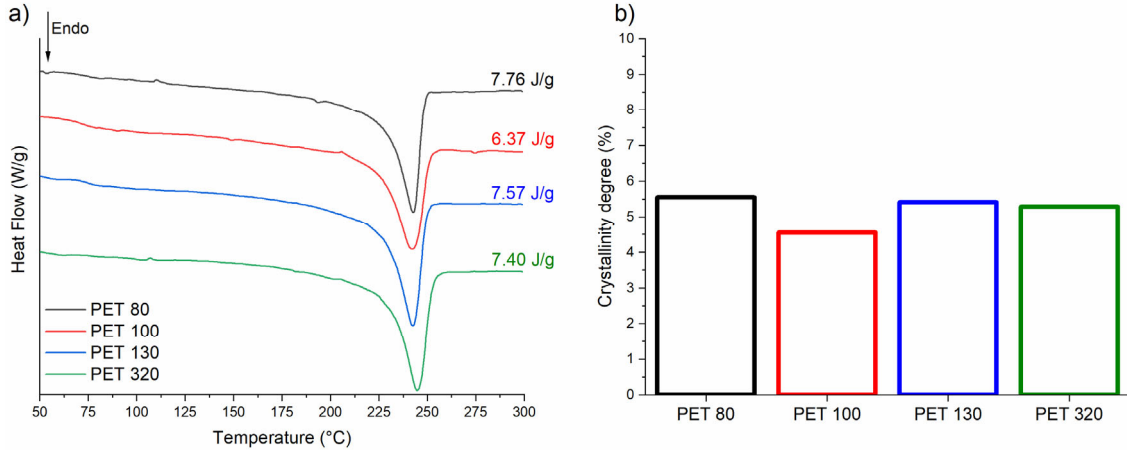
5. Results

5.1 Gas Pycnometer

Figure 2 reports the main results obtained from gas pycnometer analysis. The measured apparent densities ($\rho^*_{Measured}$) are systematically higher than the nominal ones: the straight line represents the perfect correspondence between nominal apparent density ($\rho^*_{Nominal}$) and the measured one. As a matter of fact, during sample preparation some closed cells were inevitably broken and opened due to the cutting action of the band saw. Moreover, helium gas was used to improve the sensibility and the precision of the technique employed to determine the real volume of the specimen. Thanks to the very low dimension of a helium atom (in the order of hundreds of picometers), it is possible to detect any defect that is present in the sample under analysis (e.g. not perfectly closed cells which create a percolation path for the gas). Nevertheless, although these phenomena are expected to produce a deviation in the same direction of what was observed in the data, they cannot explain the relatively large discrepancy between nominal and measured densities. It is thus obvious to conclude that the nominal values indicated by the producer are not truly representative of the actual samples under investigation; this claim is supported by the very good reproducibility of the data highlighted in Figure 2, since the error bars are smaller than the symbols representing the mean measured values.
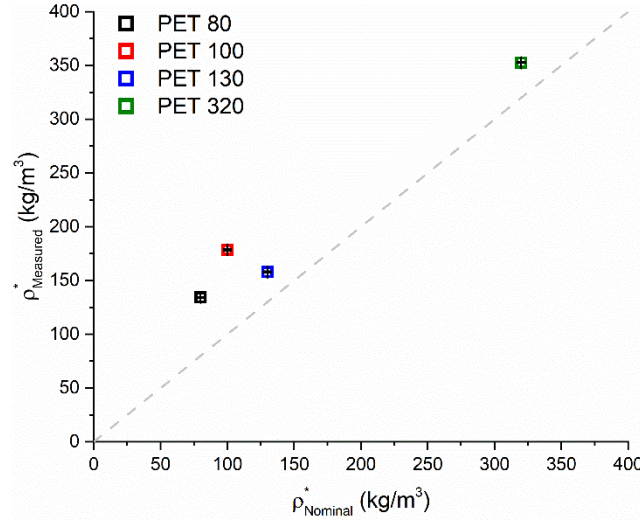
Fig. 2 Results obtained with gas pycnometer analysis in terms of apparent measured density (y-axis) versus nominal apparent density (x-axis); the dashed line represents the ideal correspondence between the two values

5.2 Differential Scanning Calorimetry

The results obtained from differential scanning calorimetry are reported in Figure 3a. Specific enthalpy values were normalized with respect to the theoretical one, 140 J/g, representing the fusion enthalpy of purely crystalline PET [36]. The crystallinity degree of the analysed material was thus obtained and shown in Figure 3b. All the samples exhibit a very low crystallinity degree, around 5%. This value justifies the choice of the mechanical properties used in the finite element simulation (see Table 2), which are representative of completely amorphous PET.

Fig. 3 Differential scanning calorimetry results: a) thermograms obtained for each material with the specific fusion enthalpy reported near the relevant curve; b) crystallinity degree evaluated normalizing the specific enthalpy with the theoretical value of 140 J/g, representing a purely crystalline PET [36]

11

5.3 Compression tests

Nominal stress ($\sigma_{nominal}$) versus nominal strain ($\varepsilon_{nominal}$) diagrams were obtained for all the mechanical tests described in the present work; nominal stress was evaluated by dividing the measured force by the original sample area and nominal strain by dividing the machine displacement, corrected by machine compliance, by the specimens' initial length. Preliminary mechanical uniaxial quasi-static compression tests, conducted up to a nominal strain of 50%, are reported in Figure 4. The stress vs. strain plot clearly highlights the peculiar mechanical behaviour of polymeric foams: a linear elastic region between 0% and about 5% strain, followed by a plateau region up to 40%, and the subsequent onset of densification regime from 40% on.
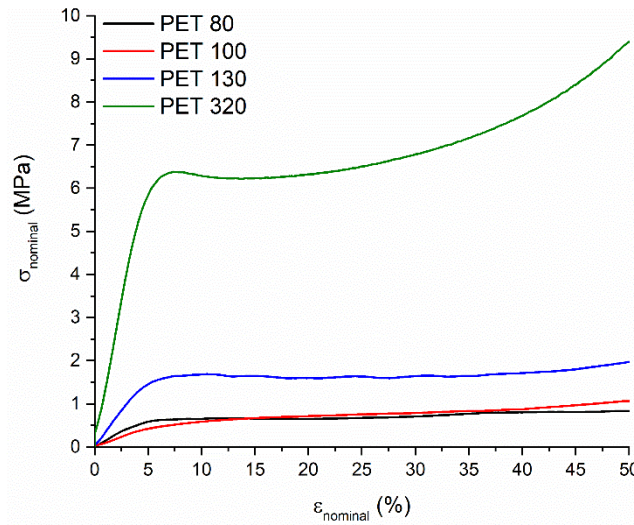

Fig. 4 Nominal stress versus nominal strain plot representing the overall mechanical response of the four polymeric foams

The results obtained from quasi-static uniaxial compression tests performed to investigate the mechanical response of cubic specimens along the three main orthogonal directions (identified as X, Y, which is the direction orthogonal to the sheet plane, and Z) are reported for all the materials in Figure 5a-d. Mean stress versus strain curves are reported, each one associated with its relevant semi-dispersion. From each test the apparent stiffness (E*) of the foam was computed as the slope of the stress-strain curve in the range between 0 and 2% of strain.
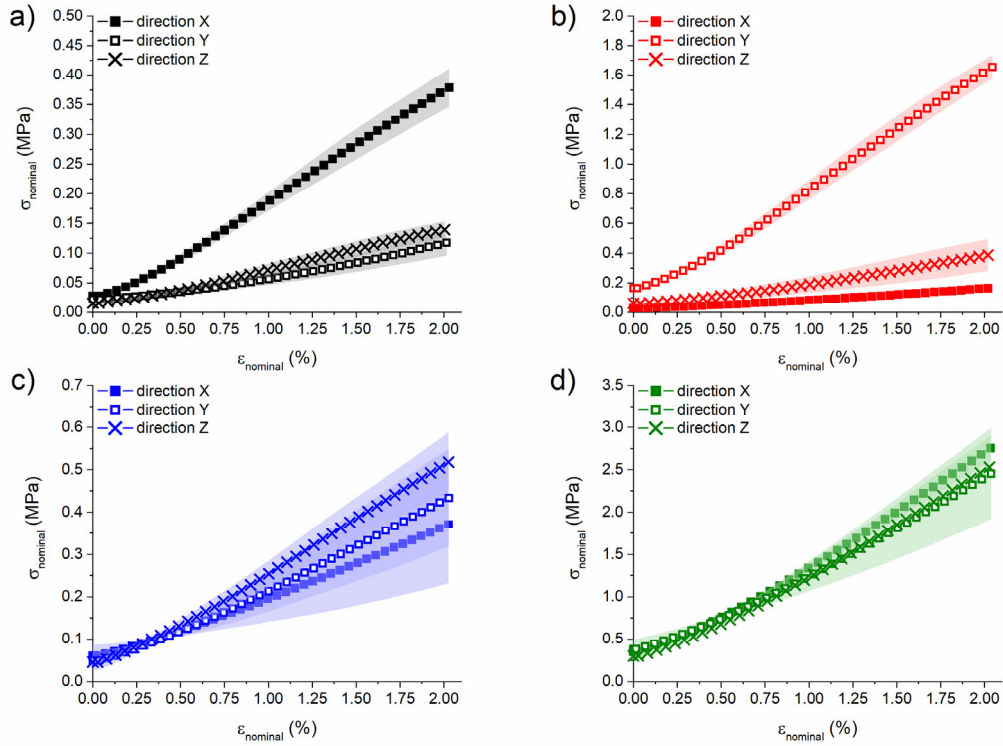
Fig. 5 Nominal stress versus nominal strain along three orthogonal directions (X, Y and Z) of the tested cubic specimens. Mean values and associated dispersions are reported for each material: a) PET 80, b) PET 100, c) PET 130 and d) PET 320; **please note that different scales are used for the four samples**

Figure 6 summarizes the values obtained for the moduli along the three orthogonal directions. The results show that the mechanical response of the specimen becomes more and more isotropic with increasing density. This phenomenon is mainly attributed to the internal structure of the specimen which becomes more isotropic as the density increases, and so does the resulting mechanical response.
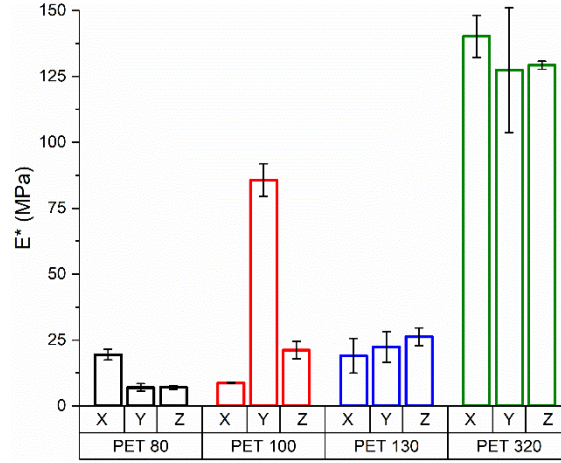
Fig. 6 Apparent stiffness (E^*) along three orthogonal directions (X, Y and Z). Mean values and mean absolute errors are reported

5.4 Structure analysis

The tomographic analysis gave an accurate reconstruction and characterization of the foam samples. In Figure 7 the cross sections taken along the X-Z plane (sheet plane) of the different samples, as cut from the material sheets, are shown. Two samples are shown for each density, both typically sharing a distinctive appearance. There are some qualitative differences between sample A and B for PET 80 and PET 130. Sample PET 80 A exhibits a densification area, not present in sample B, which also influences the shape of neighbouring cells; a similar feature is present in both samples of PET 100. On the other hand, sample PET 130 B possesses a slightly coarser structure when compared to its counterpart. While the difference observed for the two samples of PET 80 is probably fortuitous, in general variations in structure within different regions of the same sheet can occur, as demonstrated by PET 130 A and PET 130 B.

The repeatability of the tomographic analysis was ascertained through the evaluation of relevant structural parameters: solid volume fraction (Φ), mean structure thickness, mean equivalent pores diameter (D_{eq}) - i.e. the diameter of an equal volume spherical particle - and pores sphericity – i.e. the ratio of the surface areas of an equal volume sphere and that of the selected pore. The comparison of these computed quantities is reported in Figure 8 for all tested samples. For a more homogeneous comparison among all the samples, the wall thickness and the volume fraction were measured with the caution to exclude the densification areas. Had this been not the case, the average thickness and the volume fraction would have become larger; for example, as regards the average thickness, the values would have been equal to 32.1 µm (instead of 23.6 µm), 33.1 µm (instead of 25.2 µm), 25.8 µm (instead of 22.0 µm) for PET 100 A, PET 100 B, and PET 80 A, respectively.

14
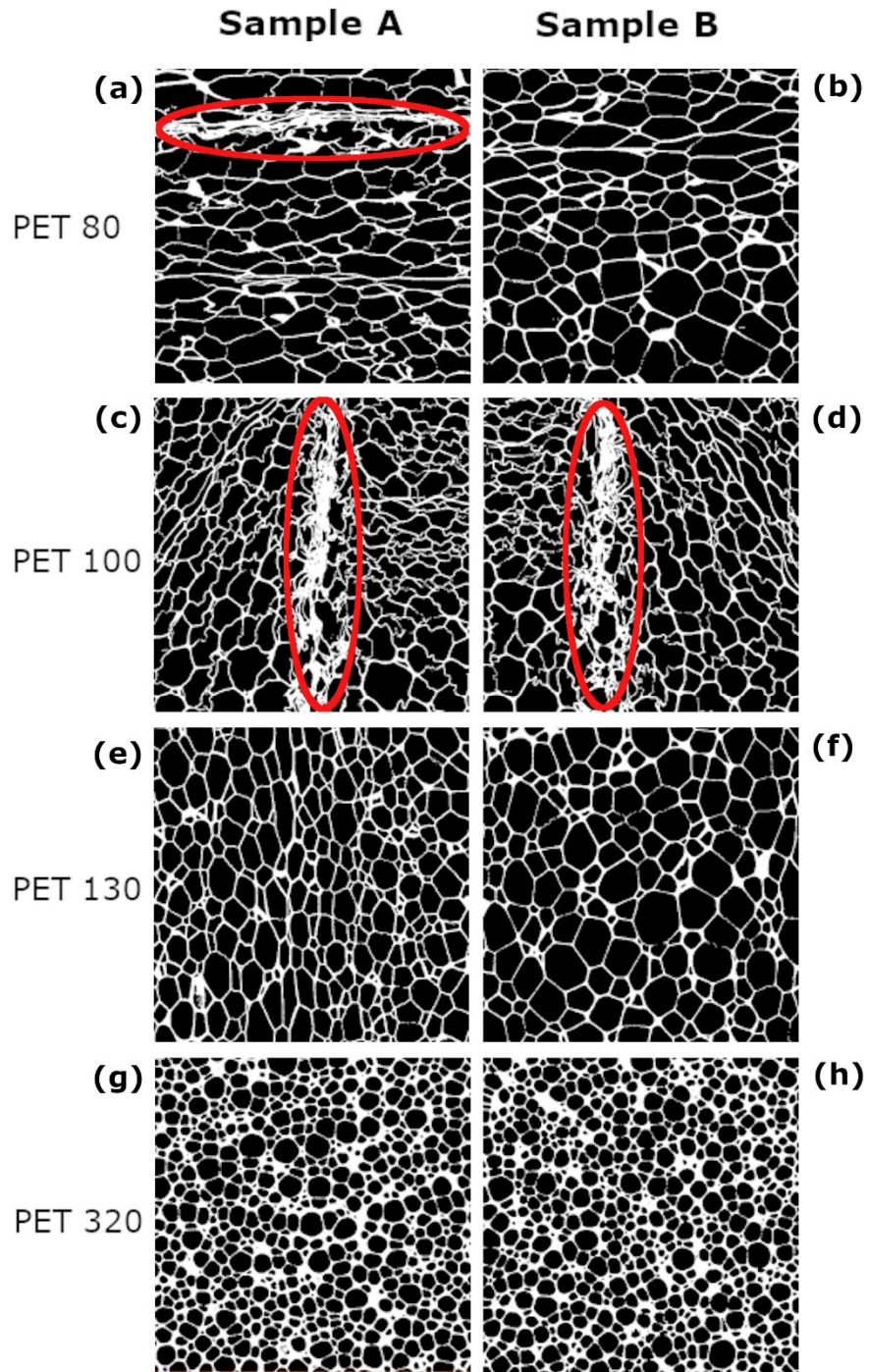
Fig. 7 Tomographic cross sections, related to the X-Z plane of observation, for all the specimens inspected with the X-Ray Computed Tomography; densification regions are highlighted with red ellipses
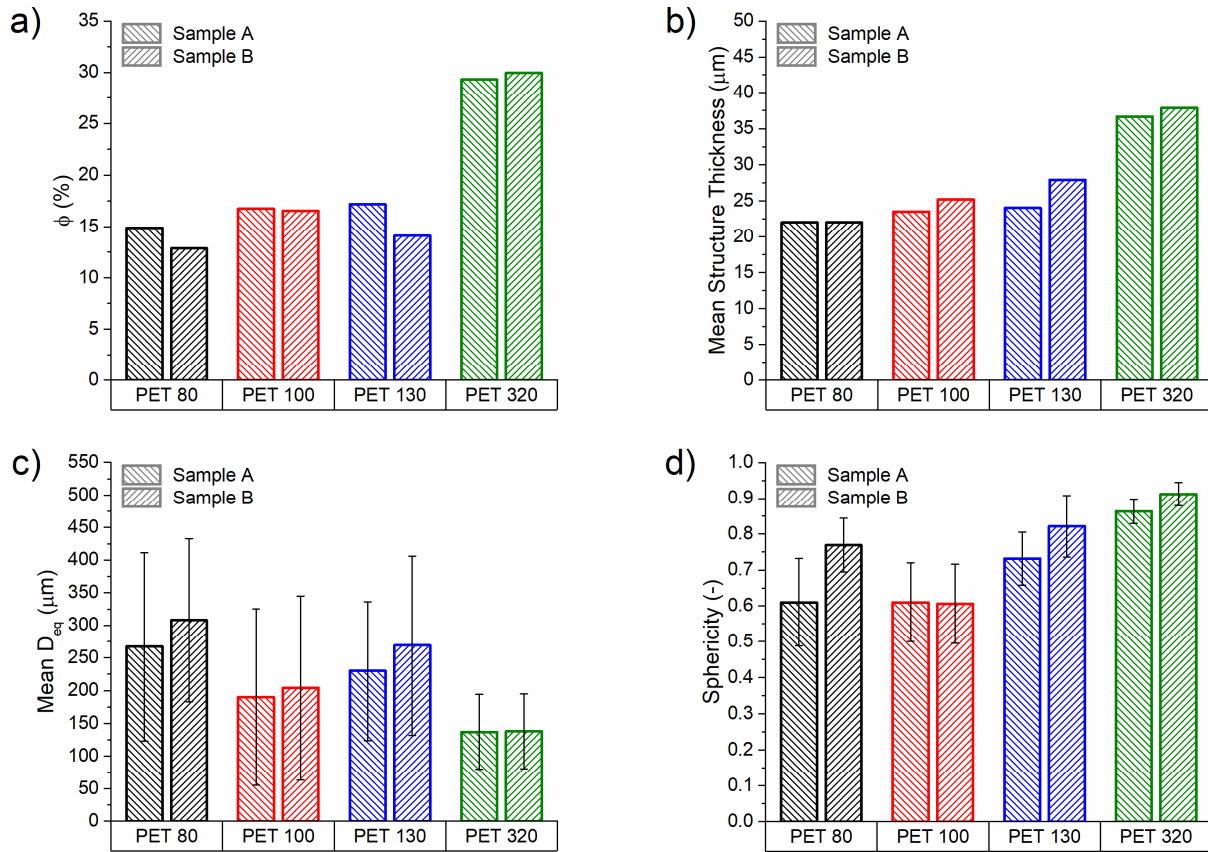
Fig. 8 Comparison of structural parameters obtained from CT for two samples of the four investigated foams: a) solid volume fraction, b) mean structure thickness, c) mean equivalent pores' diameter (D_{eq}) and d) pores' sphericity. The dispersion reported comes from the statistical analysis performed on the pores

All foams gave similar results (about 15%) in terms of solid volume fraction, with the exception of PET 320 for which a nearly double value was found; the repeatability between samples of the same foam is very good for PET 100 and PET 320, while a minor difference is observed in the case of the two other materials, probably due to the aforementioned densification areas.

The average thickness was calculated using the algorithm proposed by Hildebrand and Ruesgsegger [18] and implemented in *ImageJ*; again, the largest difference was observed between PET 320 and the other three foams. Cell diameter and sphericity measurements were taken using the Labelling analysis tool of Avizo, as already mentioned in section 3.3. The number of cells analysed for each sample is reported in Table 3 and from statistical analysis the dispersions reported in Figure 8c and 8d were computed. A larger relative variation of properties was reported for the populations of PET 80, PET 100 and PET 130, with a greater dispersion in terms of equivalent diameter than cell sphericity. Again, it was mainly PET 320 that stood out of the rest, its cells being in general smaller and more spherical.

Table 3 Number of cells analysed for each sample inspected with X-Ray Computed Tomography

| Sample	Number of cells
PET 80 A	1635
PET 80 B	1402
PET 100 A	3087
PET 100 B	2626
PET 130 A	3125
PET 130 B	1928
PET 320 A	16678
PET 320 B	16541

Given the high ratio between the size of the analysed volume (about four millimetres) and typical cell size (a few hundred micrometres), the concentrated parameters extracted from this structural analysis are considered representative of the whole structure. It is meaningful then to seek correlations between these structural parameters and other quantities.

As a first step, the solid volume fraction was related to macroscopic apparent densities, exploiting the fact that the same samples were inspected with CT and gas pycnometer analysis.

Figure 9 shows relevant data in a double logarithmic plot: a linear relationship can be identified between the apparent density and the solid volume fraction, which would lead to the following Equation 7:

$$\frac{\rho^*}{\rho_s} \approx (\Phi)^m \qquad \text{with m = 1.185} \tag{7}$$

where ρ^* is the measured apparent density, ρ_s is the reference solid density (1345 kg/m^3 for an amorphous PET), Φ is the solid volume fraction quantified from the CT scans and m is the slope of the dashed line shown in Figure 9, obtained with a linear fit.
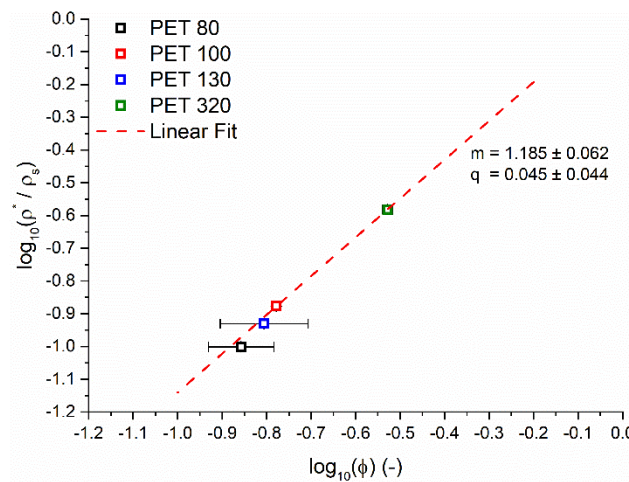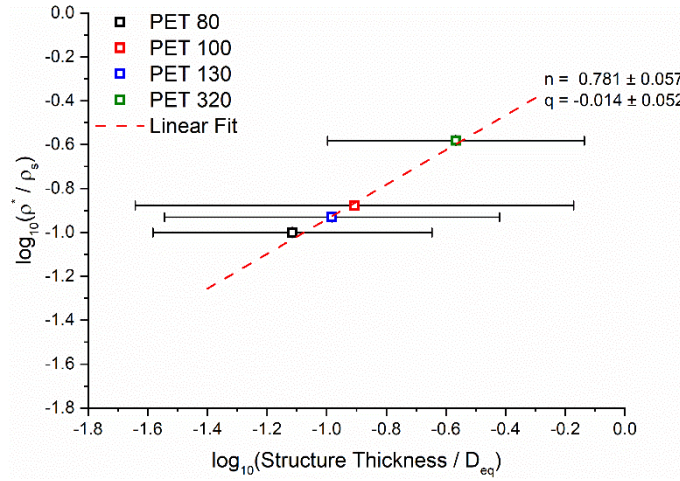

Fig. 9 Double logarithmic plot of the relative density (y-axis) versus solid volume fraction of the four foams investigated; the dashed line represents a linear fit of the data

Another relationship was found between the relative density and the ratio between the mean structure thickness and the equivalent diameter of the pores; this characteristic dimension of the cells had

already been proposed by Gibson and Ashby [13]. Also, in this case a linear fit of the data (shown in Figure 10) was performed. A relationship similar to the one reported in equation number 7 could thus be identified:

$$\frac{\rho^*}{\rho_s} \approx \left(\frac{Structure\ Thickness}{D_{eq}}\right)^n \qquad \text{with n = 0.781} \qquad (8)$$

where ρ^* is once again the measured apparent density, ρ_s is PET solid density, D_{eq} is the mean equivalent diameter of the measured pores and n is the slope of the dashed lines reported in Figure 10.

Fig. 10 Double logarithmic plot of the relative density (y-axis) versus the ratio of mean structure thickness and the equivalent diameter of the pores; the dashed line represents a linear fit of the data

Both linear fits were accomplished with an r^2-value greater than 0.99, indicating that the identified relationships can be considered valid from a statistical point of view.

The other main analysis performed on the image set concerns the global anisotropy of the samples investigated. This task was accomplished through the methods presented in the theoretical background chapter (MIL and ACF).

The results of anisotropy analysis for all the examined samples are graphically summarized in Figure 11 which reports the values of the degree of anisotropy (DA) evaluated with both MIL and ACF algorithms. The three eigenvalues (λ_i) and the direction of the corresponding eigenvectors, where Θ is the inclination angle and φ the azimuth, are reported in the supplementary information section. In general, a strong agreement between the data computed by ACF and by MIL is evident and there is also a good repeatability between the two samples A and B. The ACF method gives a degree of anisotropy constantly higher than MIL, in accordance with the findings of Wald [33]. The reported results also show that the degree of anisotropy is inversely correlated with the nominal density of the foams, confirming the considerations highlighted in the compression tests results; the mechanical response of the materials becomes more and more isotropic with the increase of the density, due to a more homogeneous and isotropic structure of the cells. Both PET 320 samples (A and B) are characterized by small and more spherical cells and have a degree of anisotropy close to one, while PET 80 and PET 100 samples, with the smallest density and the most elongated cells, present the

largest anisotropy value. A graphical representation based on Rose diagrams of the analysis results is visible in Figure 12. In each diagram, the three eigenvectors of the tensor are also depicted in light blue colour, with their length proportional to the corresponding eigenvalues.
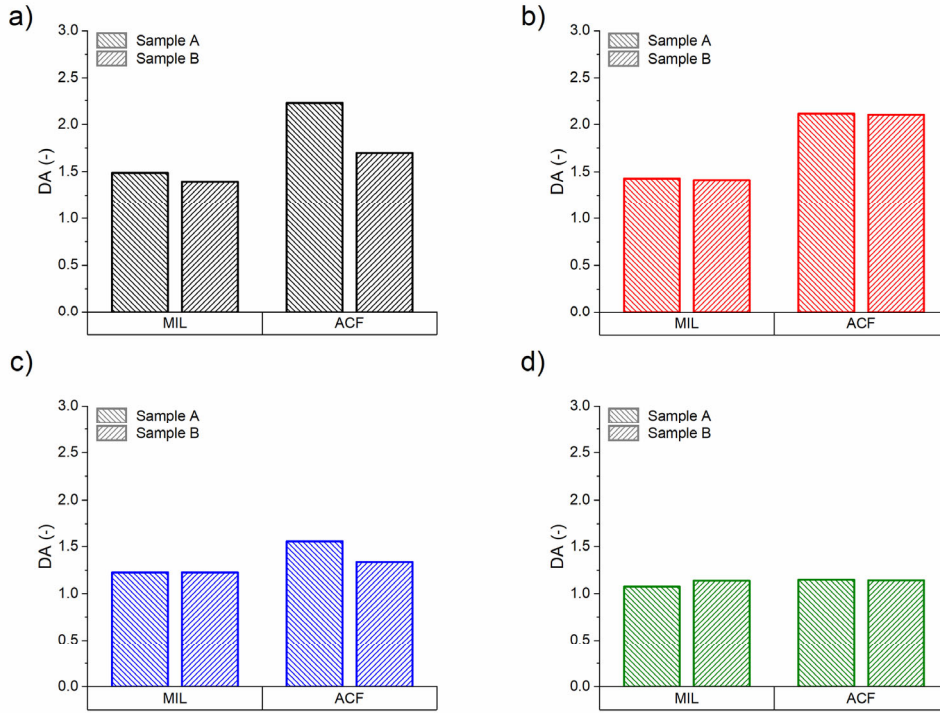

Fig. 11 Comparison of degree of anisotropy index (DA) evaluated with both MIL and ACF algorithms for each inspected sample: a) PET 80, b) PET 100, c) PET 130 and d) PET 320

Finally, the version of the MIL algorithm proposed by Wald[1] [33] to calculate the wall thickness along the different orientations, Th(w), was applied to sample PET 320 A, whose fabric tensor revealed a more isotropic structure with respect to the other foam samples. The obtained average value:

$$Th_{avg} = \frac{1}{N} * \sum_{w=1}^{N} Th(w) = 39.1 \ \mu m \tag{9}$$

agrees well with the one computed previously using the Hildebrand algorithm (see Figure 8); this result is not surprising, given the very isotropic structure possessed by the sample. It's interesting to point out that the same measurement performed using the ACF algorithm delivered a very similar result:

$$Th_{avg} = \frac{1}{N} * \sum_{w=1}^{N} FWHM(w) = 38.4 \mu m \tag{10}$$

---

[1] For each direction of the test lines, Wald computed a bone mean intercept length (BMIL) as the average of the distance between a bone entry point and the subsequent bone exit point. The BMIL is then an estimate of the average value of the foam wall thickness in the different directions.

The analysis just performed would make little sense if applied on the other foams, because the latter show a more marked anisotropy and the summation in the equation 9 and 10 could no longer be directly interpreted as an average thickness value.
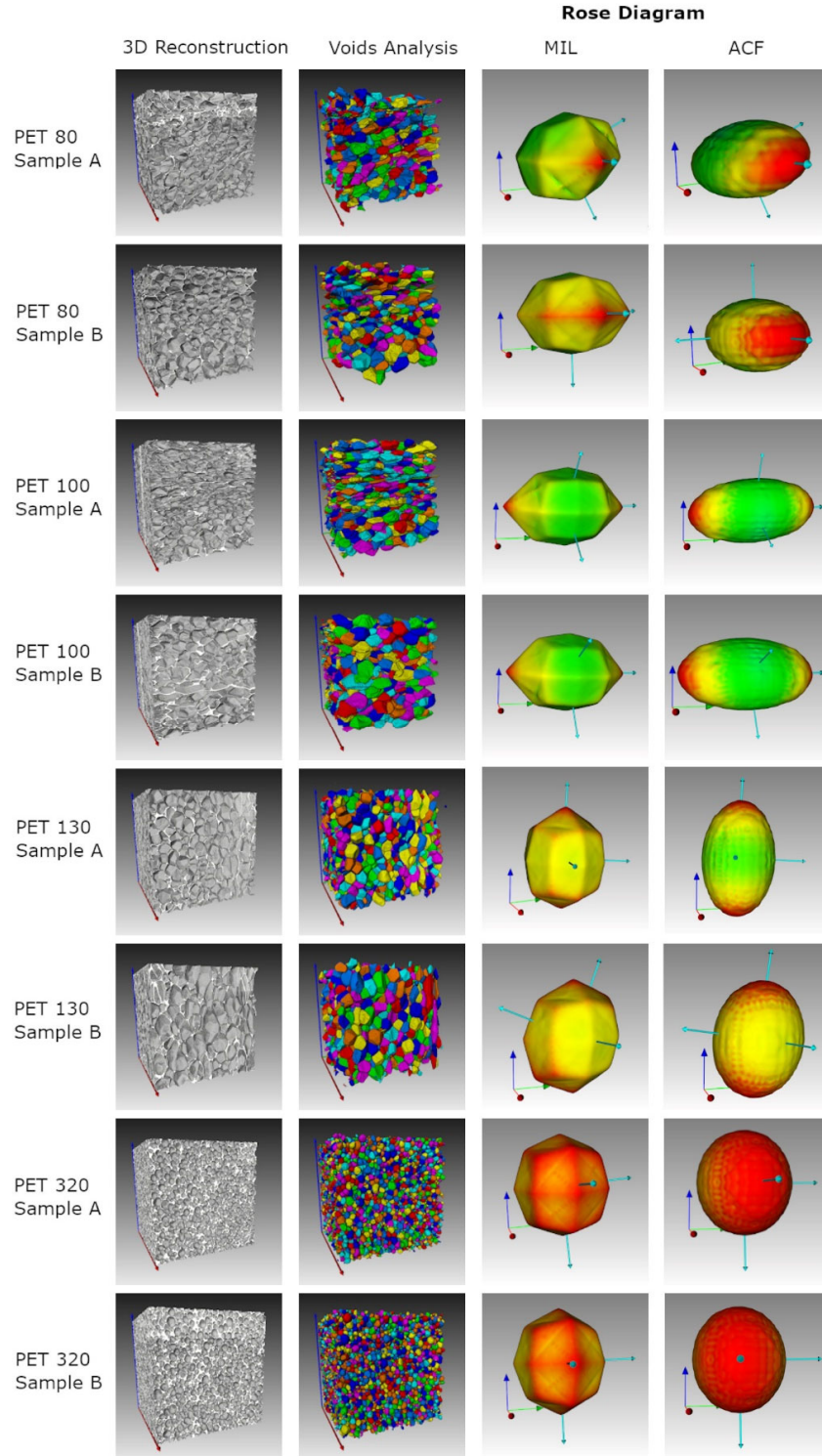
Fig. 12 Graphical representation of anisotropy analysis results in terms of Rose diagrams, which represent the orientation of the structure in a cartesian 3D coordinate system. Diagrams are reported for all the investigated samples for both MIL and ACF analyses

5.5 Mesh optimization and reconstruction

Mesh optimization is a crucial aspect of image-based approaches which are aimed at converting ~~to~~ the set of images, acquired from X-Ray CT analysis, into a finite element mesh that represents the real structure of the sample scanned. Figure 13 shows the effectiveness of the new custom-made developed algorithm in greatly reducing the number of elements required to reconstruct the entire volume inspected with the tomography. The number of elements is plotted as a function of Peano's number and threshold variation (Th), the two parameters of the adopted algorithm. Data in the graph refer to sample PET 320 A, but similar results were obtained for the other samples as well.
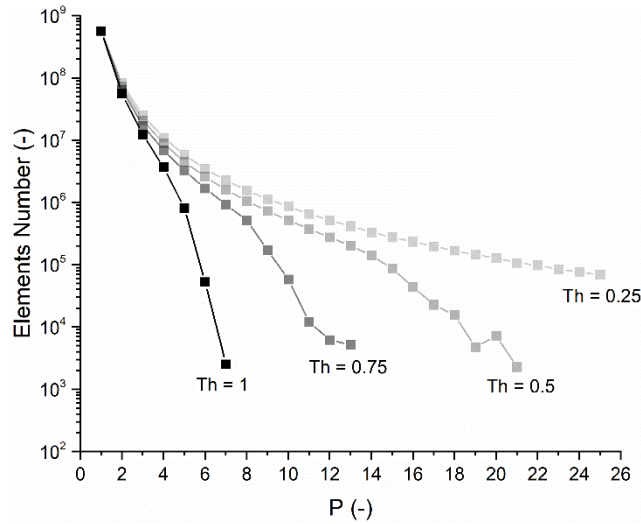
Fig. 13 Total number of elements required to reconstruct the entire volume inspected with X-Ray CT as a function of Peano's algorithm parameters: threshold (Th) tuning and Peano's number (P).

The reduction of the number of elements required to reconstruct the geometry must be achieved while at the same time preserving the essential morpho-structural characteristics of the relevant inspected sample. Figure 14 clearly shows how it is possible, with proper tuning of the two aforementioned parameters, to maintain the final values of the morpho-structural characteristics of the specimen close to their original ones. Considering the reported example (with data obtained from sample PET 320 A), the choice of values 10 for P and 0.5 for Th ensures that relevant structural parameters are not varied by more than 5% with a sensible reduction of the element number by three orders of magnitude, from 568973091 to 520081. The main advantage of the proposed algorithm resides in the very limited required computational resources. Its accuracy is strictly related to the quality of the original image: the higher its initial resolution, the higher the effectiveness of the algorithm in reducing the elements number without altering too much the morphological characteristics of the inspected sample.
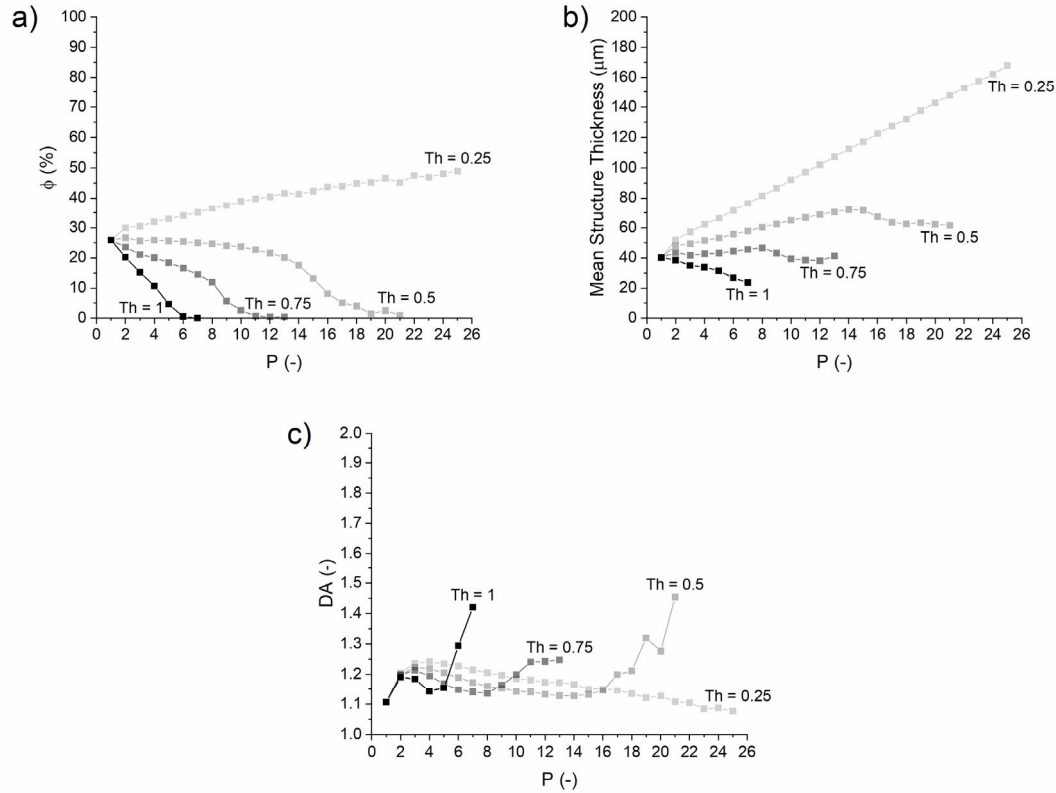
Fig. 14 Effect of Peano's algorithm variables on the main morpho-structural parameters of sample PET 320 A: a) solid volume fraction (Φ); b) mean structure thickness; c) degree of anisotropy (DA)

After the application of Peano's algorithm the resulting volume is subsequently processed with the marching cubes one to convert it into a finite element mesh; this result represents an ideal compromise between the number of elements and faithfulness to the original morpho-structural characteristics. The resolution of the marching cube algorithms matches that of the image set reduced using Peano's. An example of finite element mesh reconstruction is reported in Figure 15; the geometries shown refers to sample A of each density.

The optimally tuned parameters of the Peano's algorithm are reported in Table 4 for each sample, together with the element number before and after its application; new final resolution used in the marching cubes algorithm is also listed.

Table 4 Results of mesh optimization performed by applying Peano's algorithm using the listed optimal parameters. The spatial resolution of the original set of images was 3 μm.

Sample	Original number of elements	Reduced number of elements	P	Th	Modified resolution [μm]
PET 80 A	369997393	323934	10	0.4	30
PET 80 B	282556706	318097	10	0.4	30
PET 100 A	456845460	345770	10	0.5	30
PET 100 B	470968553	402227	10	0.5	30
PET 130 A	377427402	297431	10	0.5	30
PET 130 B	308986233	343174	10	0.5	30
PET 320 A	643671877	599183	10	0.5	30
PET 320 B	658234174	629510	10	0.5	30
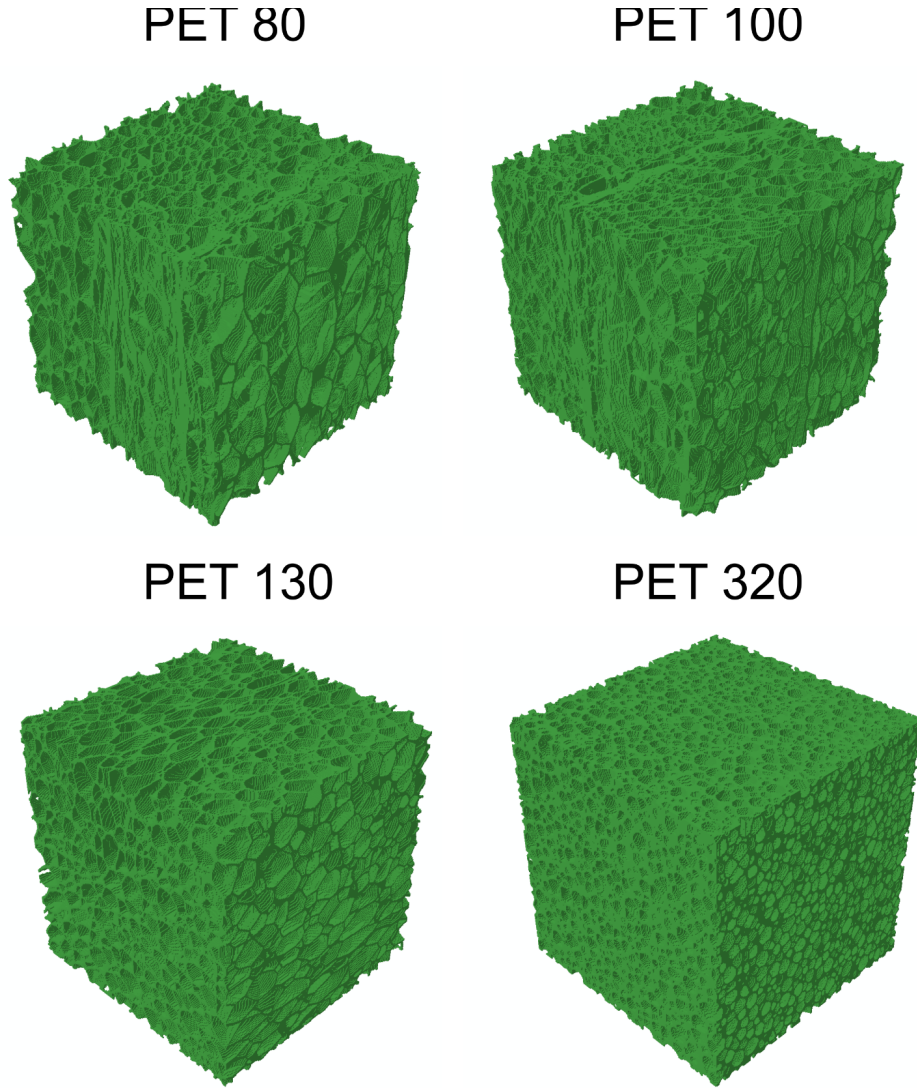
Fig. 15 Finite element mesh reconstruction after the application of Peano's algorithm to the set of images obtained through tomography. All the geometries shown refers to sample A of the corresponding density

Figure 16 summarizes the comparison of the original and modified (after application of Peano's algorithm) morpho-structural characteristics. It is clear that only minor variations in terms of solid volume fraction (Φ) and degree of anisotropy occurred; the main difference between the original and reduced size structures is in the mean structure thickness. Obviously, the reduction of the spatial resolution is accompanied by a coarser representation of existing structures: the thinner ones are either deleted or made thicker. Nevertheless, a good tuning of Peano's parameters preserves the essential features of the investigated structure (as detected by the high-resolution CT scan) even in this coarser reproduction, which in turn allows a huge reduction in the total element number (about three orders of magnitude). This reduction is necessary to reduce the computational burden of the analysis to levels which are compatible with the currently available resources (in terms of RAM and CPU).
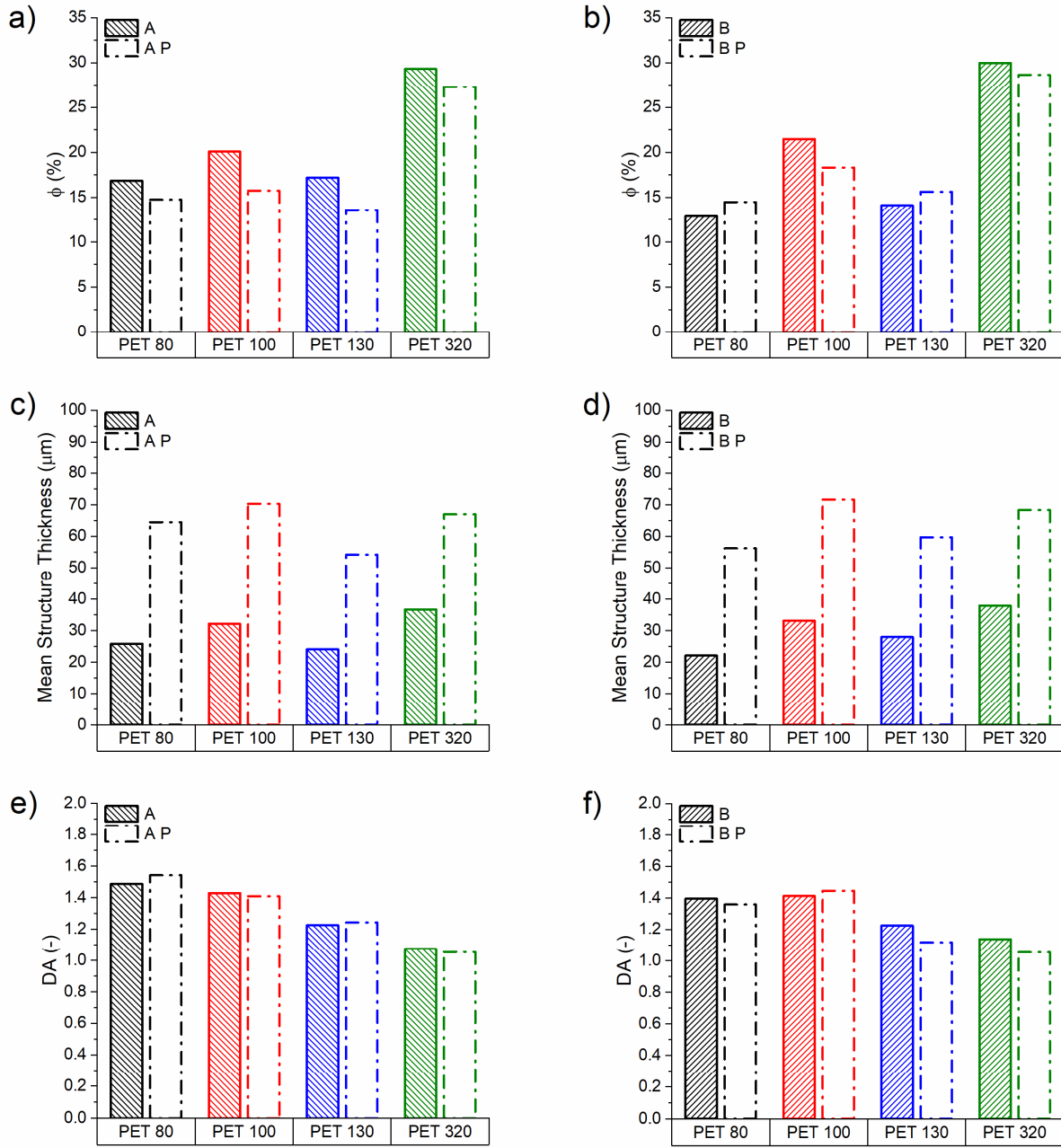
Fig. 16 Comparison between morpho-structural characteristics before and after application of Peano's algorithm; comparison is done for sample A (a), c) and e)) and B (b), d) and f)) for each density. Solid volume fraction (Φ) (a) and b)), mean structure thickness (c) and d)) and degree of anisotropy (DA) (e) and f)) are reported.

Peano's algorithm, besides its ability to generate reduced structures from real CT scans, can also be exploited to generate fictitious structures by artificially altering the algorithm's parameters. In this study 12 fictitious structures were generated starting from the real PET 320 to broaden the range of structures to be analysed beyond the limits enforced by the currently available foaming techniques. In real foams, it is very difficult to control single parameters of the final structure obtained, with changes in the production process typically influencing several parameters at once. The generation of fictitious structures allows to single out the individual contribution of each morphological feature

to the macroscopic mechanical properties of the foam. In the present work, this capability was aimed at generating structures spanning a much broader range of solid volume fraction with respect to the real ones.

5.6 Finite Element analysis

Numerical simulations of the mechanical testing of the reconstructed meshes were performed according to the experimental methods described previously. Relevant results focused on the determination of the foams' apparent stiffness (E^*), determined as the slope at the origin of the nominal stress versus nominal strain plot.
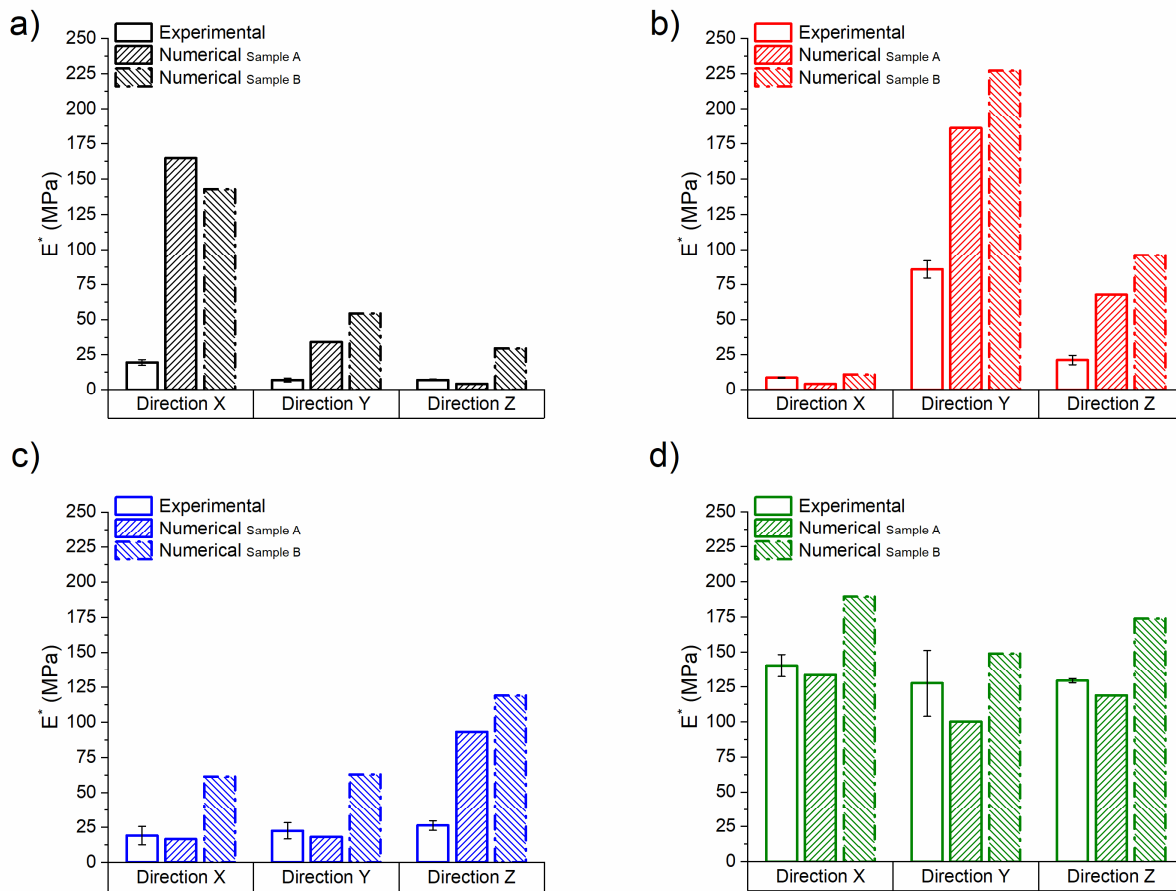

Fig. 17 Comparison between experimental apparent stiffness and numerical apparent stiffness evaluated along three orthogonal directions (X, Y and Z) for each investigated sample: a) PET 80, b) PET 100, c) PET 130 and d) PET 320. Experimental data shows average values and dispersion of five samples for each foam density; for the numerical simulations, individual results obtained for each reconstructed sample are shown.

In Figure 17 a comparison is made between the experimental data, obtained along three orthogonal directions on all tested samples, and those obtained from the numerical ones on the reconstructed geometries representing the originally inspected samples (2 for each density). It is clear from the graph that in some cases the numerical results overestimate the experimental ones and reasons explaining this fact will be discussed in the next section. Despite this mismatch, the numerical results confirm many of the previously obtained results. The degree of anisotropy apparent from stiffness

data decreases with increasing density of the foams, with the moduli along the three orthogonal directions converging towards more similar values. The average apparent stiffness correctly scales with the apparent density of the foam, except for the testing directions in which unusually high values were reported (to be discussed later).

These results (both experimental and numerical) were combined with those obtained by analysing the fictitious structures generated thanks to Peano's algorithm. Taking advantage of a much broader range of void volume fraction $(1 - \Phi)$ examined, a very clear bilinear trend of the apparent stiffness can be identified, as shown in Figure 18. Here the mean apparent stiffness ($E_{Mean}^* = \frac{E_X^* + E_Y^* + E_Z^*}{3}$) of each sample was normalised with respect to the reference amorphous PET bulk modulus. A marked change in slope is visible at about 80% void volume fraction, which incidentally is very close to the Φ values of the tested foams (except for PET 320, whose samples had a lower volume fraction). This very large variation in the sensitivity of the stiffness to the void volume fraction is consistent with a transition in the foam deformation mechanism from an axially dominated to a bending dominated one [10]; it is also in agreement with the general conclusion obtained by Cowin, which is based on symmetry considerations applied to orthotropic porous materials [5].
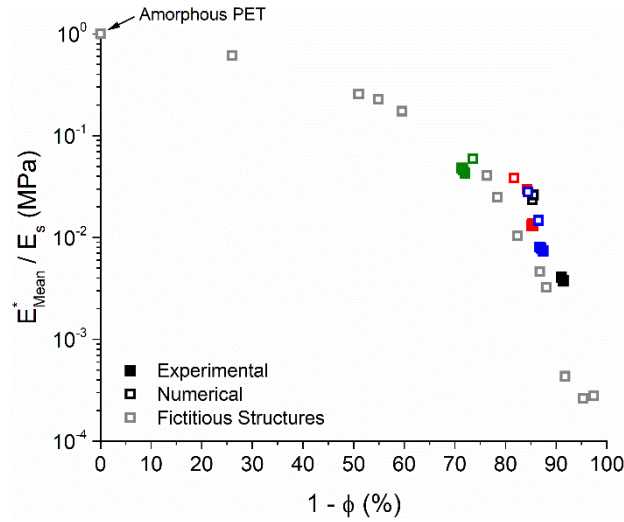
Fig. 18 Normalized mean apparent stiffness (E_{Mean}^*/E_s) as a function of void volume fraction. Filled coloured symbols represent experimental mechanical tests and empty coloured symbols are the numerical simulations performed on the structures reconstructed from the relevant images sets; empty grey symbols are the results obtained from fictitious structures

Finally, the relation between mechanically observed and structurally determined anisotropy was explored. Despite a certain degree of scatter visible in Figure 19, a good correlation was found between the ratio of maximum to minimum apparent stiffness (E_{Max}^* / E_{Min}^*) for each analysed sample and the corresponding ratio of the maximum and minimum eigenvalues ($\lambda_{Max} / \lambda_{Min}$), evaluated with both MIL and ACF algorithms. The degree of anisotropy determined directly from the analysis of the CT inspected samples can then be taken as a good indication of the expected level of mechanical anisotropy found in the material. With this respect the range of fictitious structures investigated is not very significant since they were generated from PET 320 with the objective of modifying the volume fraction and not anisotropy characteristics.

Moreover, comparing the bar graphs in Figure 17 with the ACF and MIL rose diagrams in Figure 12, it is evident that the direction of the maximum eigenvector computed from the fabric tensor is oriented in accordance with the elastic principal directions. This result confirms their mutual strict relation and supports the use of structural parameters to predict mechanical anisotropy [23, 38, 39].
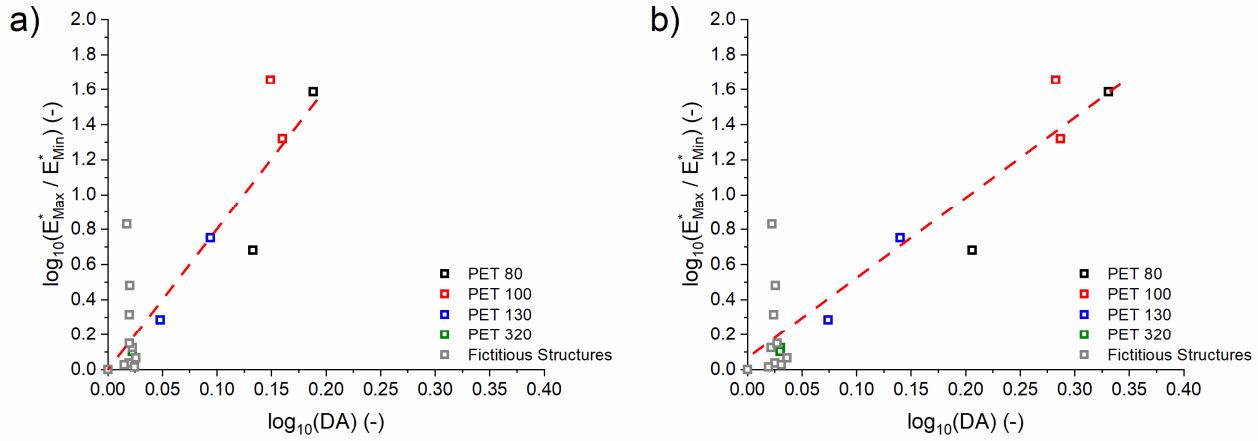

Fig. 19 Ratio of maximum to minimum apparent stiffness (E^*_{Max}/E^*_{Min}) and computed degree of anisotropy (DA): a) MIL and b) ACF. Empty coloured symbols represent numerical simulations on the structure reconstructed from images sets optimization and empty grey symbols are the results obtained from fictitious structures.

6. Discussion

The combined experimental and numerical approach proposed in the present work was proven to be very efficient in determining quantitative parameters, in terms of both structural and mechanical characteristics of expanded polymeric materials. X-ray computed tomography and the associated algorithms were, once again, the most efficient and precise approach to determine synthetic macroscopic structural parameters, including solid volume fraction, voids' characteristic dimensions, anisotropy degree of the structure and many others presented in the previous paragraphs. It was also demonstrated how these parameters can be related to other macroscopic quantities, measured with different experimental techniques, whose outcome is insensitive to specific details of the foams' structure. These general relations can be used to infer essential information about the structure of other expanded materials when X-ray computed tomography or similar expensive techniques are not available.

From another point of view the set of images provided the basic information necessary to convert the real geometry into a finite element mesh, on which numerical simulations could be performed. Thanks to the application of the developed Peano's algorithm, a relatively large volume (dozens of mm³) of the investigated samples has been efficiently reconstructed without losing the essential features of the internal structure. This larger volume well represents the global structure of the investigated foam and consequently its associated mechanical response. The other potential application of this algorithm is the possibility to generate fictitious structures, based on real ones, to broaden the range of available geometries and improve the quality of existing relationships between mechanical and structural parameters, or identify new ones. The other main advantage resides in the possibility to simulate

structures that do not physically exist (yet) thus avoiding experimental prototyping phases, which always require long time and expensive physical resources.

For what concerns the correspondence between experimental and numerically predicted mechanical properties, it is clear that in some cases the model overestimates the real mechanical behaviour of the material, especially with the lower considered densities (e.g. PET 80 and PET 100). This is mainly due to the great number of variables that affect the final results of numerical simulation, starting from the structural variability of individuals samples; furthermore, the application of the binarization and Peano's algorithms introduces small changes in the structure whose effect on lighter foams is relatively more important. All these factors combined with the very high sensitivity of the effective stiffness to void fraction, especially in the range above 80% (Figure 18), limit the ability of the model to closely match experimental data. In fact, Figure 18 shows that even a 2% increase in the void fraction is enough to reduce the apparent stiffness by almost 3 times. A similar degree of uncertainty in the determination of the void fraction can easily be introduced by image processing; the aforementioned 2% variation can be introduced by a 5% change in the threshold value of the segmentation operation; this, without introducing any evident issue in the obtained virtual sections. Therefore, the differences reported in Figure 17 do not conflict with the aim of developing a consistent and robust numerical tool to define general relations between the microstructure and the mechanical response. The goal is reached by the proposed approach which proved to be a good compromise between the accuracy of the analysis and the requests in terms of available physical and numerical resources (time, RAM, CPU).

7. Conclusions

In the present work a combined experimental and numerical approach is proposed to comprehensively describe the microstructure and mechanical behaviour of cellular materials. The main goal was the development of an efficient approach able to represent with a high degree of accuracy the essential features of the internal microstructure and obtain useful structural parameters to be correlated with the macroscopic mechanical response. The first objective was accomplished through the investigation of the samples via X-ray computed tomography and the application of robust algorithms to compute effective parameters such as solid volume fraction, mean structure thickness and void geometry. The material distribution in the analysed volume was also characterized by defining a suitable measure of the global anisotropy of the geometry, exploiting tensorial algorithms such as Mean Intercept Length and Autocorrelation function. Results found using both algorithms show that the degree of anisotropy seems to be inversely correlated with the nominal density of the foams, in accordance with the evidence gathered from mechanical tests.

The output of X-ray computed tomography was also the starting point for the conversion of the digitally acquired physical geometry into a finite element mesh. This was made possible by the application of the marching cube algorithm and a novel optimization algorithm (based on Peano's). Their product was a huge reduction in the number of finite elements required to reconstruct the entire volume scanned with the tomography, at the same time preserving the essential features of the original structure. This optimisation algorithm was also exploited to generate synthetic fictitious structures, with arbitrary geometrical characteristics that can significantly part from the range of parameters

experimentally available. These results were accomplished with relatively low requirements in terms of computational resources, thus enabling the faithful reconstruction of the entire representative volume of the samples investigated. The outcome of the numerical procedure was validated against experimental tests to demonstrate its robustness and accuracy.

In the end some general correlations between geometric structure and mechanical properties were proposed, as an example of the potential usefulness of the proposed approach. These results are instrumental in exploring the correspondence between these aspects of foams behaviour, improving the existing knowledge of these highly complex material systems. On the practical side, the framework developed in this research represents a highly useful tool to assist the design and optimisation of foamed products, reducing associated costs and significantly speeding up the process.

Conflicts of interest

The author(s) declared no potential conflicts of interest with respect to the research, authorship, and/or publication of this article.

Supplementary information

Detailed results obtained with MIL and ACF algorithms, graphically summarized in Figure 11, are reported in the following Table 5. The three eigenvalues (λ_i) and the direction of the corresponding eigenvectors, where Θ is the inclination angle and φ the azimuth, are reported. Eigenvectors are listed following a descending order of the corresponding eigenvalue.

Table 5 Anisotropy analysis results: degree of anisotropy, eigenvalues and eigenvectors are reported for all the investigated specimens; all the values are computed through mean intercept length and autocorrelation functions algorithms

	DA	I eigenvector (Θ, φ)	II eigenvector (Θ, φ)	III eigenvector (Θ, φ)	λ_{max}	λ_{med}	λ_{min}
			PET 80 Sample A				
MIL	1.487	(88.42°, 0.84°)	(63.53°, 91.64°)	(153.47°, 87.69°)	425.907	331.573	286.375
ACF	2.225	(88.21°, 1.53°)	(67.82°, 92.26°)	(157.74°, 87.16°)	72.634	44.205	32.637
			PET 80 Sample B				
MIL	1.395	(88.41°,5.75°)	(89.70°,95.76°)	(178.38°,16.51°)	583.664	528.576	418.419
ACF	1.698	(88.07°,1.45°)	(88.40°,271.40°)	(2.51°,141.81°)	52.269	40.586	30.782
			PET 100 Sample A				
MIL	1.429	(88.52°,89.46°)	(37.53°,357.52°)	(127.49°,0.59°)	336.913	248.922	235.791
ACF	2.111	(87.36°,89.16°)	(28.92°,354.37°)	(118.77°,0.61°)	87.178	47.926	41.293
			PET 100 Sample B				
MIL	1.412	(89.53°,91.62°)	(148.31°,2.38°)	(58.31°1.33°)	348.550	263.480	246.888
ACF	2.102	(89.01°,92.51°)	(158.22°,5.01°)	(68.25°,2.12°)	94.823	56.394	45-108
			PET 130 Sample A				
MIL	1.225	(5.06°,146.28°)	(91.03°,68.00°)	(85.04°,338.09°)	355.922	297.295	290.599
ACF	1.554	(4.66°,139.76°)	(91.78°,72.16°)	(85.69°,342.30°)	56.256	37.929	36.203
			PET 130 Sample B				
MIL	1.224	(21.29°,93.75°)	(68.76°,278.01°)	(91.44°,7.45°)	574.447	524.876	469.473
ACF	1.336	(7.95°,98.62°)	(82.12°,286.02°)	(91.01°,15.88°)	56.582	46.635	42.352
			PET 320 Sample A				
MIL	1.073	(81.51°,1.77°)	(171.09°,19.58°)	(87.31°,92.17°)	174.569	170.255	162.740
ACF	1.148	(88.14°,1.21°)	(177.59°,40.57°)	(88.47°,91.26°)	57.606	56.033	50.197
			PET 320 Sample B				
MIL	1.138	(89.67°,351.31°)	(178.60°,67.69°)	(88.64°,81.31°)	204.650	200.029	179.862
ACF	1.140	(89.54°,344.61°)	(178.08°,60.93°)	(88.13°,74.63°)	61.329	59.914	53.810

References

1. ASTM D6226 (2015) Standard test method for open cell content of rigid cellular plastics
2. BS EN ISO 11357-3 (2018) Plastics – Differential scanning calorimetry (DSC) – Part 3: Determination of temperature and enthalpy of melting and crystallization
3. Andena L, Caimmi F, Leonardi L, Nacucchi M, De Pascalis F (2019) Compression of polystyrene and polypropylene foams for energy absorption applications: a combined mechanical and microstructural study, J. of Cell. Plast. 55, https://doi.org/10.1177/0021955X18806794
4. Bocciarelli M, Carvelli V, Mariani S, Tenni M (2020) Assessment of the shock adsorption properties of bike helmets: a numerical/experimental approach, Computer Methods in Biomech. and Biomed. Eng. 23, https://doi.org/10.1080/10255842.2019.1709451
5. Cowin SC (1985) The relationship between the elasticity tensor and the fabric tensor, Mech. of Mater. 4(2):137–147
6. Cowin SC (1986) Wolff's law of trabecular architecture at remodeling equilibrium, J. of Biomech. Eng. 108(1):83-88
7. Cowin SC, Doty SB (2007) Tissue Mechanics. Springer, New York USA
8. De Pascalis F, Nacucchi M, Scatto M, Albertoni R (2016) Quantitative characterisation of low density, high performance polymeric foams using high resolution X-ray computed tomography and laser confocal microscopy, NDT & E Int. 83:123–133
9. De Pascalis F, Nacucchi M (2019) Relationship between the anisotropy tensor calculated through global and object measurements in high-resolution X-ray tomography on cellular and composite materials, J. of Microsc. 273:65-80, https://doi.org/10.1111/jmi.12762
10. Deshpande VS, Ashby MF, Fleck NA (2001) Foam topology bending versus stretching dominated architectures, Acta Mater. 49:1035-1040
11. Fazekas A, Dendievel R, Salvo L, Brechet Y (2002) Effect of microstructural topology upon the stiffness and strength of 2D cellular structures, J. of Mech. Sci. 44:2047-2066
12. Fischer F, Lim GT, Handge UA, Altstädt V (2009) Numerical simulation of mechanical properties of cellular materials using computed tomography analysis, J. of Cell. Plast. 45, https://doi.org/10.1177/0021955X09339340
13. Gibson LJ, Ashby MF (2002) Cellular solids structure and properties, 2nd edition, Cambridge Solid State Science Series
14. Gong L, Kyriakides S, Jang WY (2005) Compressive response of open-cell foams. Part I: Morphology and elastic properties, Int. J. of Solids and Struct. 42:1355-1379
15. Gong L, Kyriakides S (2005) Compressive response of open-cell foams. Part II: Initiation and evolution of crushing, Int. J. of Solids and Struct. 42:1381-1399
16. Gong L, Kyriakides S, Triantafyllidis N (2005) On the stability of Kelvin cell foams under compressive loads, J. Mech. Phys. Solids 53:771-794
17. Harrigan T, Mann RW, (1984) Characterization of microstructural anisotropy in orthotropic materials using a second rank tensor, J. of Mater. Sci. 19(2):761–767
18. Hildebrand T, Rüesgsegger P (1997) A new method for the model-independent assessment of thickness in three-dimensional images, J. of Microsc. 185(1):67–75
19. Jacobs LJM, Kemmere MF, Keurentjes JTF (2008) Sustainable polymer foaming using high pressure carbon dioxide: a review on fundamentals, processes and applications, Green Chem. 10:731-738, https://doi.org/10.1039/B801895B
20. Ketcham RA, Ryan TM (2004) Quantification and visualization of anisotropy in trabecular bone. J. of Microsc., 213(2):158–171
21. Lorensen WE, Cline HE (1987) Marching cubes: a high-resolution 3D surface construction algorithm. Computer Graph. 21(4):163-169

22. Moreno R, Borga M, Smedby Ö (2014) Techniques for computing fabric tensors: a review. In: Westin, C.F., Vilanova, A., Burgeth, B. (eds) Visualization and Processing of Tensors and Higher Order Descriptors for Multi-Valued Data. Springer, Berlin, Heidelberg Germany

23. Odgaard A, Kabel J, Van Rietbergen B, Dalstra M, Huiskes R (1997) Fabric and principal directions of cancellous bone are closely related. J. Biomech. 30:487–496

24. Odgaard A (2001) Quantification of cancellous bone architecture. In: Cowin, S.C. editor. Bone Mechanics Handbook, Boca Raton, FL: CRC Press LLC, chapter 14

25. Roberts AP, Garboczi EJ (2001) Elastic moduli of model random three-dimensional closed-cell cellular solids, Acta Mater. 49:189-197

26. Rodriguez-Perez MA, Alvarez-Lainez M, de Saja JA (2009) Microstructure and physical properties of open-cell polyolefin foams, J. Appl. Polym. Sci. 114:1176-1186, https://doi.org/10.1002/app.30283

27. Sauceau M, Fages J, Common A, Nikitine C, Rodier E (2011) New challenges in polymer foaming: a review of extrusion processes assisted by supercritical carbon dioxide, Prog. in Polym. Sci. 36:749-766, https://doi.org/10.1016/j.progpolymsci.2010.12.004

28. Schroeder W, Martin K, Lorensen B (2006) Visualization Toolkit, An Object-Oriented Approach to 3D Graphics. 4th ed. Kitware Inc. ISBN: 1-930934-19-X, New York

29. Stock SR (2008) Recent advances in x-ray microtomography applied to materials, Int. Mater. Rev. 53:129-181, https://doi.org/10.1179/174328008X277803

30. Tabor Z (2009) On the equivalence of two methods of determining fabric tensor, Med. Eng. & Phys. 31(10):1313–1322

31. Tagliabue S, Rossi E, Baino F, Vitale-Brovarone C, Gastaldi D, Vena P (2017) Micro-CT based finite element models for elastic properties of glass-ceramic scaffolds, J. of the Mech. Behav. of Biomed. Mater. 65:248-255, https://doi.org/10.1016/j.jmbbm.2016.08.020

32. Trofa M, Di Maio E, Maffettone PL (2019) Multi-graded foams upon time-dependent exposition to blowing agent, Chem. Eng. J. 362:812-817, https://doi.org/10.1016/j.cej.2019.01.077

33. Wald MJ, Vasilic B, Saha PK, Wehrli FW (2007) Spatial autocorrelation and mean intercept length analysis of trabecular bone anisotropy applied to in vivo magnetic resonance imaging, Med. Phys. 34(3):1110–1120

34. Whitehouse WJ (1974) The quantitative morphology of anisotropic trabecular bone, J. of Microsc. 101(2):153-168

35. Wismans JGF, Goveart LE, van Dommelen JAW (2010) X-Ray computed tomography-based modelling of polymeric foams: the effect of finite element model size on the large strain response, J. Polym. Sci. Part B: Polym. Phys. 48:1526-1534, https://doi.org/10.1002/polb.22055

36. Wunderlich B (1990) Thermal Analysis, Academic Press, pp.417-431

37. Zhu HX, Knott JF, Mills NJ (1996) Analysis of the elastic properties of open-cell foams with tetrakaidecahedral cells, J. Mech. Phys. Solids 45:319-343

38. Zysset PK, Goulet RW, Hollister SJ (1998) A global relationship between trabecular bone morphology and homogenized elastic properties, J. Biomech. Eng. 120(5):640-646

39. Zysset PK (2003) A review of morphology-elasticity relationships in human trabecular bone: theories and experiments, J. Biomech. 36(10):1469–1485

40. Morton DT, Reyes A, Clausen AH, Hopperstad OS (2020) Mechanical response of low density expanded polypropylene foams in compression and tension at different loading rates and temperatures, Mater. Today Comm. 23, https://doi.org/10.1016/j.mtcomm.2020.100917

41. Rodriguez-Perez MA, Lobos J, Perez-Munoz CA, de Saja JA (2009) Mechanical response of polyethylene foams with high densities and cell sizes in the microcellular ranges, J. of Cell. Plast. 45:389-403

42. Huber N (2018) Connections between topology and macroscopic mechanical properties of three-dimensional open-pore materials, Materials. Front. Mater. 5(69), 10.3389/fmats.2018.00069

43. Chen W, Hao H, Hughes D, Shi Y, Cui J, Li ZX (2015) Static and dynamic mechanical properties of expanded polystyrene, Mater. and Design 69:170-180, http://dx.doi.org/10.1016/j.matdes.2014.12.024

44. Harper CA (2002) Handbook of plastics, elastomers and composites, McGraw Hill Professional 4th edition

45. The Scientist and Engineer's Guide to Digital Signal Processing, 2nd edition, by Steven W. Smith, ISBN 0-9660176-6-8

46. Tang Q, Fang L, Guo W (2019) Effects of bamboo fiber length and loading on mechanical, thermal and pulverization properties of phenolic foam composites, J. of Biores. And Bioprod. 4:51-59, https://doi.org/10.21967/jbb.v4i1.184